Vibrational and structural properties of P$_2$O$_5$ glass: Advances from a combined modeling approach

N. S. Shcheblanov,[1,*] L. Giacomazzi,[2,3] M. E. Povarnitsyn,[4] S. Kohara,[5,6,7,†] L. Martin-Samos,[3] G. Mountjoy,[8] R. J. Newport,[8] R. C. Haworth,[8] N. Richard,[9] and N. Ollier[1]

[1]*Laboratoire des Solides Irradiés CEA-CNRS, École polytechnique, F-91128 Palaiseau, France*
[2]*Materials Research Laboratory, University of Nova Gorica, Vipavska 11c, SI-5270 Ajdovščina, Slovenia*
[3]*CNR-IOM/Democritos National Simulation Center, Istituto Officina dei Materiali, c/o SISSA, via Bonomea 265, I-34136 Trieste, Italy*
[4]*Joint Institute for High Temperatures, RAS, 13 Building 2 Izhorskaya Street, Moscow 125412, Russia*
[5]*Research Center for Advanced Measurement and Characterization, National Institute for Materials Science, Hyogo 679-5148, Japan*
[6]*Center for Materials Research by Information Integration, Research and Services Division of Materials Data and Integrated System, NIMS, Ibaraki 305-0047, Japan*
[7]*PRESTO, Japan Science and Technology Agency, Tokyo 102-0076, Japan*
[8]*School of Physical Sciences, University of Kent, Canterbury CT2 7NH, United Kingdom*
[9]*CEA, DAM, DIF, Bruyères-le-Châtel, F-91297 Arpajon Cedex, France*

We present experimental measurements and *ab initio* simulations of the crystalline and amorphous phases of P$_2$O$_5$. The calculated Raman, infrared, and vibrational density of states (VDOS) spectra are in excellent agreement with experimental measurements and contain the signatures of all the peculiar local structures of the amorphous phase, namely, bridging and nonbridging (double-bonded or terminal) oxygens and tetrahedral PO$_4$ units associated with Q^2, Q^3, and Q^4 species (Q^n denotes the various types of PO$_4$ tetrahedra, with n being the number of bridging oxygen atoms that connect the tetrahedra to the rest of the network). In order to reveal the internal structure of the vibrational spectrum, the characteristics of vibrational modes in different frequency ranges are investigated using a mode-projection approach at different symmetries based on the T_d symmetry group. In particular, the VDOS spectrum in the range from ∼600 to 870 cm^{-1} is dominated by bending (F_{2b}) motions related to bridging oxygen and phosphorus (∼800 cm^{-1} band) atoms, while the high-frequency doublet zone (∼870–1250 cm^{-1}) is associated mostly with the asymmetric (F_{2s}) and symmetric (A_1) stretching modes, and most prominent peak around 1400 cm^{-1} (exp. 1380 cm^{-1}) is mainly due to asymmetric stretching vibrations supported by double-bonded oxygen atoms. The lower-frequency range below 600 cm^{-1} is shown to arise from a mixture of bending (E and F_{2b}) and rotation (F_1) modes. The scissors bending (E) and rotation (F_1) modes are well localized below 600 cm^{-1}, whereas the F_{2b} bending modes spread further into the range ∼600–870 cm^{-1}. The projections of the eigenmodes onto Q^2, Q^3, and Q^4 species yield well-defined contributions at frequencies in striking correspondence with the positions of the Raman and infrared bands.

I. INTRODUCTION

The phosphate glass family exhibits many attractive properties depending on the glass composition. In particular, phosphate glasses possess excellent optical properties and ion exchangeability and fiber drawing ability [1,2]. Furthermore, phosphate glasses can sustain a high rare-earth ion loading, enabling us to produce compact laser sources and amplifiers in fiber form [3]. Not only that, at variance with silica-based glasses, phosphate glasses have suitable photo-darkening properties [4,5]. Despite the importance of P$_2$O$_5$ glasses in industry and nature and the many theoretical and experimental studies of P$_2$O$_5$ phases [6–13], spectroscopic observations pertinent to the optical and vibrational properties are few [14–17]. This may explain to some extent why no consensus exists yet about the structure and vibrations of

pure P$_2$O$_5$ glass [10]. The power of Raman and infrared (IR) spectroscopies for investigating glasses has been recognized by many scientists. However, in order to fully exploit these vibrational spectroscopies, it is necessary to possess a reliable theoretical modeling approach to correctly interpret the relevant features of the vibrational spectra. By contrast, to our knowledge, a mode assignment in vitreous P$_2$O$_5$ (v-P$_2$O$_5$) has been explored by numerical simulations for only specific cluster models [14,15,17,18]. Essentially, it was implied that the typical features of the Raman spectrum of v-P$_2$O$_5$ are three bands [14–19]: (i) the phosphoryl stretch band, whose maximum is at ∼1380 cm^{-1}, (ii) the symmetric stretch of the bridging oxygen band at ∼640 cm^{-1}, and (iii) the bending mode band appearing at a lower-frequency range of 300–500 cm^{-1}. However, the cluster model approach is hardly applicable in network glasses due to the impossibility to account for the cooperative effects, the description of which requires more realistic glass models which allow for a proper treatment of long-range effects [20–26]. Thus, until now, there have not been any available theoretical investigations of vibrational
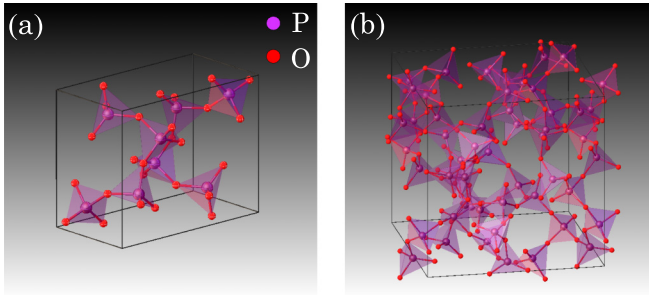
*n.s.shcheblanov@gmail.com
†skohara@icloud.com

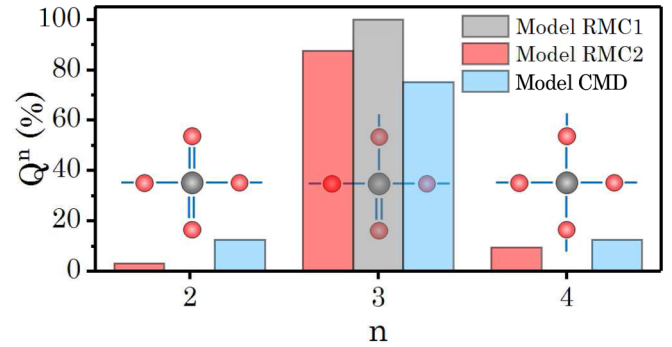FIG. 1. (a) Elementary cell of o'-P_2O_5 [27]. (b) The network of the v-P_2O_5 RMC1 model.

FIG. 2. Q^n distribution of v-P_2O_5. Distributions are presented for RMC1/RMC2 models obtained by Kohara's RMC approach [35,36] and for the CMD model obtained by classical MD [29]. Q^n species for the PO_4 structural unit are shown schematically in the inset.

spectra relying on realistic models of the v-P_2O_5 network that can provide the attributions of vibrational modes.

In this paper, we generate realistic v-P_2O_5 models and present a comprehensive analysis of vibrational spectra based on *ab initio* simulations, the mode-projection approach, and comparison with experimental measurements of vibrational spectra, which allows us to perform a consistent mode assignment of the Raman, IR, and vibrational density of states (VDOS) spectra in v-P_2O_5.

II. SIMULATION METHODS AND STRUCTURAL PROPERTIES

The pure v-P_2O_5 network is expected to comprise tetrahedrons with three bridging oxygen bonds (P–O–P), which share a maximum of three of their corners with neighboring tetrahedra, while the fourth bond represents double-bonded (terminal) oxygen (P=O) unconnected to other tetrahedral units (see Fig. 1); that is, the v-P_2O_5 network contains Q^3 tetrahedral units in terms of the Q speciation [6,28], where Q^n denotes PO_4 tetrahedra, with n being the number (between 2 and 4) of bridging P–O–P linkages per tetrahedron. Usually, the classical molecular dynamics (CMD) and reverse Monte Carlo (RMC) approaches are applied to simulate glasses, and models generated by these approaches provide satisfactory agreement with experiments on structure factor. However, despite many studies dedicated to v-P_2O_5 [8,9,29–34], up to now, it was not possible to generate v-P_2O_5 models with more than 75% of Q^3 units. Recently, Kohara *et al.* developed a hybrid RMC approach which opened the door to confidently treat glass systems, providing new insights into the structural properties [35–37]. Owing to these advances, we generate three models with 112 atoms: two RMC models (hereafter labeled RMC1 and RMC2) and one CMD model. RMC modeling is performed using the RMC++ code [35–37]. The difference between the RMC1 and RMC2 models lies in the different constraints that were applied in RMC calculations. For the case of the RMC1 model, the constraints on the P–O connectivity are that 32 phosphorus atoms ought to be coordinated by one nonbridging (terminal) oxygen atom at 1.4–1.5 Å (in total 32 nonbridging oxygen atoms) and three bridging oxygen atoms at 1.5–1.7 Å (in total 48 bridging oxygen atoms), whereas, for the case of the RMC2 model, the constraint on coordinations is not applied. The atomic number density for P_2O_5 glasses is 0.0708 Å^{-3}. The final RMC run

is conducted under these constraints by fitting to both x-ray and neutron total structure factors $S(q)$ [8]. In particular, the structure of RMC1 and RMC2 have the highest proportions of Q^3 units ever reported, being 100% and 87.5%, respectively (see Fig. 2). Such a distribution plays an essential role in our research due to the strong sensitivity of vibrational spectra to local symmetry. We follow Ref. [29] in order to generate the CMD model, and the simulations are carried out with the help of the LAMMPS code [38].

Figures 3(a) and 3(b) show good agreement of the glass models with the experimental measurements of the structure factor with neutron [7] and x-ray [8] diffraction; however, the RMC models give better agreement. One can note that for $q \lesssim 2.5$ Å^{-1}, i.e., corresponding to length scales beyond nearest-
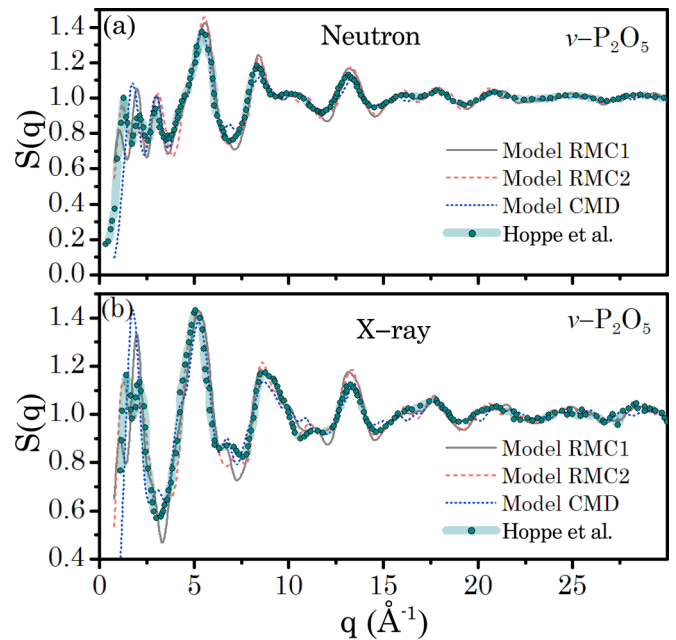

FIG. 3. Dependence of the (a) neutron and (b) x-ray static structure factor on magnitude of momentum transfer for v-P_2O_5. Models RMC1 (solid gray curve), RMC2 (dashed red curve), and CMD (dotted blue curve) and experimental data for neutrons [7] and x rays [8] (shaded dotted green curve) are shown.
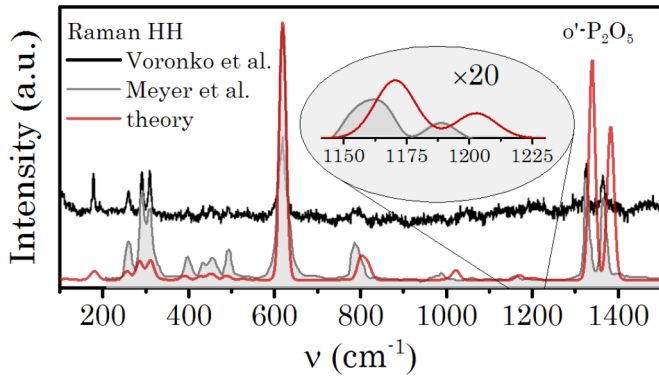
FIG. 4. Reduced Raman horizontal-horizontal (HH) spectra of o'-P_2O_5: theory (solid red curve), experimental data by Meyer et al. [45] (solid gray curve), and experimental data by Voron'ko et al. [46] (solid black curve). A Gaussian broadening (8 cm^{-1}) is used for the theoretical curve.

neighbor distance, both neutron and x-ray $S(q)$ show a kind of double peak at 1.3 and 2.3 Å^{-1}, which is not resolved by the CMD model, while to some extent it is resolved by both the RMC models. Moreover, the RMC2 model counterintuitively seems to provide a slightly better agreement for $q \lesssim 2.5$ Å^{-1} with experiments, even though it has Q^2 and Q^4 units [8]. Thus, it appears evident that relying only on the structural information provided by the structural probes such as neutron and x-ray scattering may constitute a severe limitation for advanced modeling of pure v-P_2O_5. Crucial complementary information can, however, be obtained by means of vibrational spectroscopies. However, a detailed understanding of the vibrational spectra can be achieved only through accurate theoretical modeling. Such a high level of accuracy requires theoretical approaches which address the electronic structure directly. In this context, first-principles calculations based on density functional theory (DFT) are particularly appealing for a good compromise between accuracy and computational cost. All the calculations carried out in this work are based on the DFT. In particular, a generalized gradient approximation (GGA) (i.e., the Perdew-Burke-Ernzerhof functional) and local density approximation (LDA) exchange-correlation functional are adopted for the DFT calculations included in Ref. [39]. Norm-conserving Troullier-Martins and Bachelet-Hamann-Schlüter pseudopotentials are used for O and P atoms, respectively [40,41]. Kohn-Sham wave functions are expanded in a basis of plane waves up to a kinetic cutoff of 70 Ry. The wave functions are expanded at the sole Γ point of the Brillouin zone, as justified by the large size and the large band gap of our system. Geometry optimizations are obtained by means of a two-step relaxation procedure (TSP): first, a spin-polarized GGA optimization, followed by a further LDA relaxation of the atomic structure. As the CMD provides configurations that are slightly far from a DFT ground state, a gradient-corrected functional is preferred in the first step to accelerate the convergence of the algorithm. The second optimization step is required in view of an accurate calculation of vibrational modes, as LDA is known to reproduce vibrational frequencies in better agreement with experiments than GGA [13,42]. In both optimization steps, the minimum is found by

adopting a force threshold of 0.0025 eV/Å, which allows for proper harmonic treatment of the vibrational modes. When applied to the CMD model, the TSP provides a structure lower in energy by 0.03 eV/atom with respect to a direct LDA relaxation. The former TSP relaxed structure features a decrease by 3% of Q^2 and Q^4 units and an increase of 6% of Q^3 units with respect to the structure relaxed directly in LDA. In contrast, as far as RMC1, which has only Q^3 units, is concerned, the TSP relaxed structure is equivalent to a direct LDA relaxation (difference in energy $\leqslant 0.0005$ eV/atom) with no change in the network topology; that is, in both cases, the relaxed structure consists of only Q^3 units. Calculations of the vibrational modes of relaxed CMD and RMC models are obtained by exploiting a linear response approach [43]. The codes used for the present calculations of structural and vibrational properties are freely available with the QUANTUM ESPRESSO package [44].

III. RESULTS AND DISCUSSION

First, we demonstrate the reliability of our DFT calculation scheme by calculating the Raman spectrum for a crystalline phase, o'-P_2O_5 [27] (see Fig. 1). As we can see in Fig. 4, the theoretical Raman spectrum very closely resembles the experimental one. All signatures are reproduced, including a fine structure in the 100–550-cm^{-1} frequency range. A small shift of $\sim 1\%$ with respect to experimental data at higher frequencies represents the accuracy limit of the present DFT calculations in agreement with recent calculations for phosphosilicate glasses [13]. Thus, we can rely on the DFT approach to consider v-P_2O_5 vibrational spectra. In Fig. 5(a), we can see that all v-P_2O_5 models reproduce two main experimental Raman peaks (~ 640 and ~ 1380 cm^{-1}) and one moderate band at ~ 800 cm^{-1}. However, only the RMC1 model resembles the experimental spectrum over the whole range, while the CMD and RMC2 models produce quite strong additional features at high frequencies (~ 1000–1300 cm^{-1}) compared to the silent doublet [~ 950 and ~ 1150 cm^{-1} (experiment: ~ 920 and ~ 1110 cm^{-1})]. Considering the IR spectra in Fig. 5(b), we can mention that only the RMC1 model provides very good agreement with the experimental spectrum and reproduces all signatures (~ 450, ~ 800, ~ 950, ~ 1100, and ~ 1380 cm^{-1}), whereas the CMD and RMC2 models do not reproduce the peak position of the central band, ~ 800 cm^{-1}; deform and shift the strongest, ~ 950 cm^{-1}, band; and generate additional features at high frequencies similar to Raman spectra.

In Fig. 5(c) we present the VDOS analysis. The experimental VDOS was obtained using the inelastic neutron scattering technique with experimental details as reported elsewhere [48]. We can see that, apart from the very beginning, <100 cm^{-1} (boson peak area), and the double-bonded oxygen line, 1400 cm^{-1} (experiment: 1380 cm^{-1}), all models exhibit similar qualitative behavior and reproduce the main experimental features: (i) mid-frequency bands at ~ 450, ~ 650, and ~ 800 cm^{-1} and (ii) high-frequency bands at ~ 950, ~ 1150, and ~ 1380 cm^{-1}. The origin of the slight shift of the 1380 cm^{-1} line comes from the DFT calculation in the case of oxide glasses, as mentioned above. The broad range of wave numbers used in the neutron experiments does
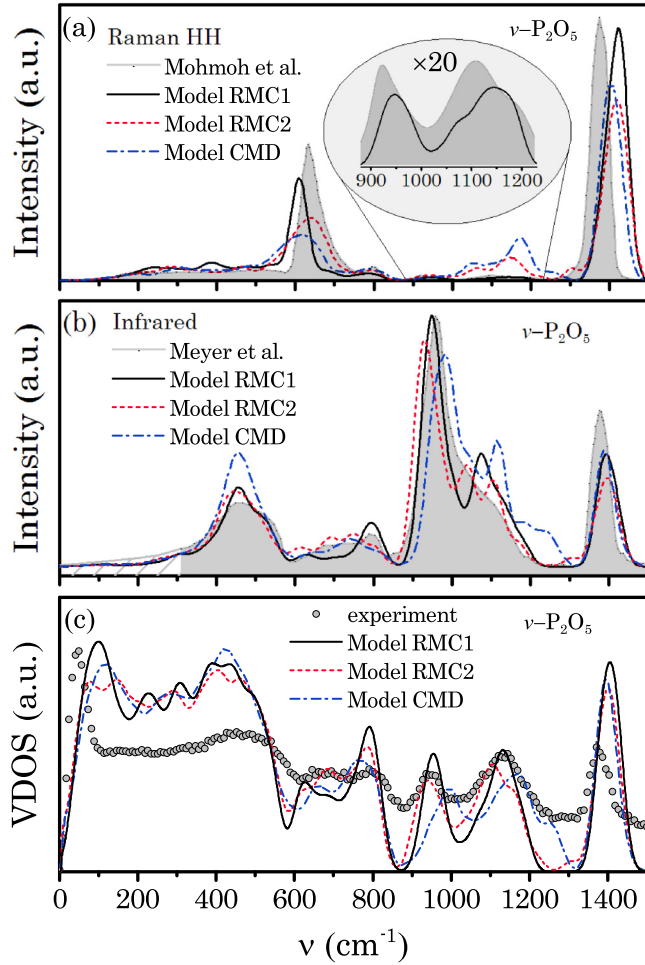
FIG. 5. Vibrational spectra of v-P_2O_5. (a) Reduced Raman HH spectra with experiment by Mohmoh *et al.* [16], (b) IR absorption spectra with experiment by Meyer *et al.* [47], and (c) VDOS spectra with experiment (present work). In all panels, experiment, solid gray curve; the RMC1 model, solid black curve; the RMC2 model, dashed red curve; and the CMD model, dot-dashed blue curve. A Gaussian broadening (20 cm^{-1}) is used for all theoretical curves.

not resolve accurately the boson peak area; however, this circumstance does not affect the present vibrational analysis. Despite the qualitative similarity of the simulation and experimental spectra, however, there are significant differences in the structure of simulation spectra. In particular, the CMD model shifts the high-frequency spectrum ($\sim$950 and $\sim$1150 cm^{-1}) by $\sim$100 cm^{-1}, essentially deforming it in relation to RMC and experimental spectra. In addition, the RMC2 model shifts the mid-frequency band ($\sim$650 cm^{-1}) and the high-frequency band ($\sim$1150 cm^{-1}). By contrast, a comparison of the experimental and *ab initio* RMC1 model VDOS spectra shows very good agreement over the whole frequency range, reproducing the exact locations of all the main features. Thus, similar to Raman and IR spectra, the CMD and RMC2 models deform VDOS spectra, inducing additional features at high frequencies [see Fig. 5(c)]. In order to reveal these features, we decompose the VDOS spectra in terms of Q^n species by projecting vibrations onto
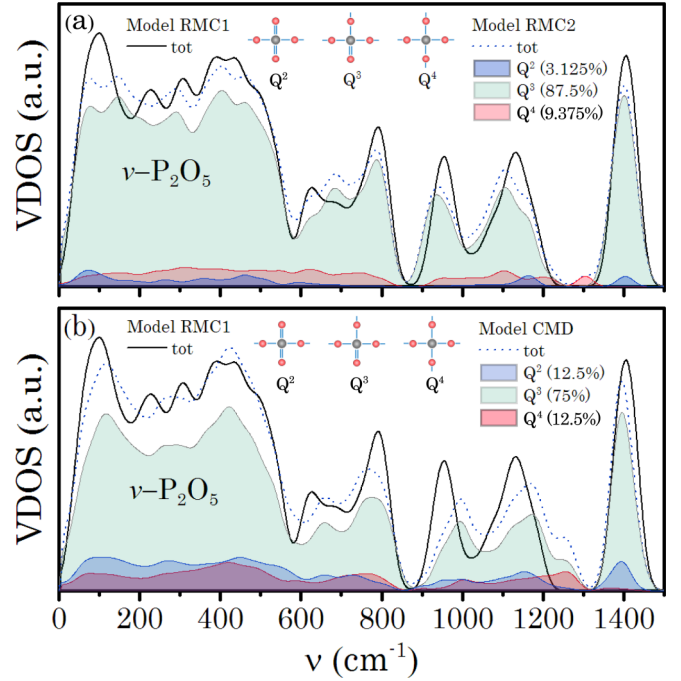

FIG. 6. The partial VDOS for Q^n species: (a) the RMC1 model vs the RMC2 model (b) and the RMC1 model vs the CMD model. Q^n species for PO_4 structural unit are shown schematically in the inset. Note that the RMC1 model has 100% Q^3 units.

corresponding Q^n structural units:

$$Z(\nu) = \sum_{n=2}^{4} Z_n(\nu) = \frac{1}{3N_{at}} \sum_n \sum_k \sum_{I_n} \left| \mathbf{e}_{I_n}^k \right|^2 \delta(\nu - \nu_k), \quad (1)$$

where the index k labeling the vibrational modes runs from 1 to $3N_{at}$, N_{at} is the total number of atoms in the models (112 atoms), $\mathbf{e}^k$ and ν_k are eigenmodes and eigenfrequencies, the index I_n runs over the Q^n units, and

$$\left| \mathbf{e}_{I_n}^k \right|^2 = \left| \mathbf{e}_{P_n}^k \right|^2 + \sum_{i_{TO} \in Q^n} \left| \mathbf{e}_{i_{TO}}^k \right|^2 + \frac{1}{2} \sum_{i_{BO} \in Q^n} \left| \mathbf{e}_{i_{BO}}^k \right|^2, \quad (2)$$

where P_n denotes phosphorus atoms belonging to I_n units and i_{BO} and i_{TO} enumerate bridging and terminal oxygen atoms within Q^n units. Figures 5(c), 6(a), and 6(b) show clearly that the Q^2 and Q^4 units (in CMD and RMC2 models) deform VDOS spectra at $\sim$600–1450 cm^{-1} and hence induce corresponding differences in Raman and IR spectra with respect to experimental measurements and the RMC1 model. Thus, the RMC1 model, comprising only Q^3 units, provides excellent agreement with all the experimental measurements and properly represents the structure of pure v-P_2O_5. The additional features at high frequency in all vibrational spectra are the signatures of Q^2 and Q^4 units in the network of CMD and RMC2 models (see Fig. 2), supporting previous experimental Raman studies [19] on Na-doped P_2O_5 containing Q^2 units.

Previous research based on the specific cluster model [14,15,17] was able to confidently assign only the high-frequency Raman and IR band 1380 cm^{-1}, ascribing it to the motion of the double-bonded oxygens along the P=O bonds. Since high-frequency modes are quite localized
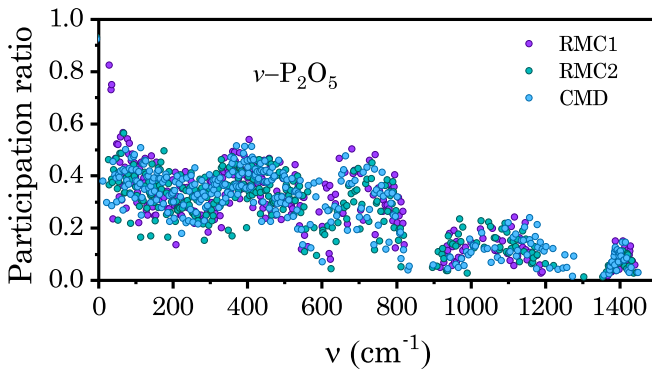
FIG. 7. The dependence of the participation ratio on frequency for the RMC1 (violet circles), RMC2 (green circles), and CMD (blue circles) models.

(having a participation ratio (PR) of ∼0.2; see Fig. 7), cluster models [14,15,17] are capable of explaining their nature. However, the medium-frequency range (∼300–870 cm^{-1}) is characterized by a quite strong cooperative effect (in fact, modes are rather nonlocalized, having PR ∼0.5; see Fig. 7), and cluster models can hardly be applied. We overcome the cluster model limitations by using the 112-atom models (RMC and CMD). To better understand the internal structure of vibrations, we perform a projection analysis in terms of the chemical species. In Fig. 8(a), the VDOS spectrum projected onto species reveals a quite noticeable coupling of phosphorus and oxygens atoms at ∼600–870 cm^{-1}, a uniform moderate presence of phosphorus motion at frequencies below ∼600 cm^{-1}, suppressed phosphorus activity in the high-frequency doublet zone (∼870–1250 cm^{-1}) with respect to the bridging oxygens, and considerable phosphorus gain in the narrow ∼1400 cm^{-1} band. The doublet zone can be attributed mostly to the bridging oxygens, while the terminal oxygens provide only a negligible contribution. By contrast, the ∼1400 cm^{-1} band (experiment: 1380 cm^{-1}) is practically forbidden for the bridging oxygens, mostly arising from terminal oxygen motions. Some very interesting Raman features relate to the frequency range between ∼550 and 700 cm^{-1} [see Fig. 5(a)], where a strong Raman enhancement is observed at ∼610 cm^{-1} (experiment: 640 cm^{-1}). Umari and Pasquarello developed an approach for the decomposition of Raman spectra [49,50]; however, their approach does not take into account the interference effect between specific groups of atoms or vibration, which does not provide the decomposition of the spectra in an additive manner. We adapt this approach to take into account the interference effect to decompose the Raman spectrum into partial contributions of specific groups of atoms, i.e., P atoms, terminal oxygen (TO) atoms, and bridging oxygen (BO) atoms (see the legend in Fig. 8), to fully represent the total spectrum (see the Appendix). As a result, the Raman horizontal-horizontal (HH) intensity is a sum of three terms:

$$\mathcal{I}(\nu) = \mathcal{I}_P(\nu) + \mathcal{I}_{TO}(\nu) + \mathcal{I}_{BO}(\nu). \quad (3)$$

By projecting the VDOS onto phosphorous and terminal and bridging oxygen atoms, we can see that in the range ∼550–700 cm^{-1} bridging oxygen motions are dominant
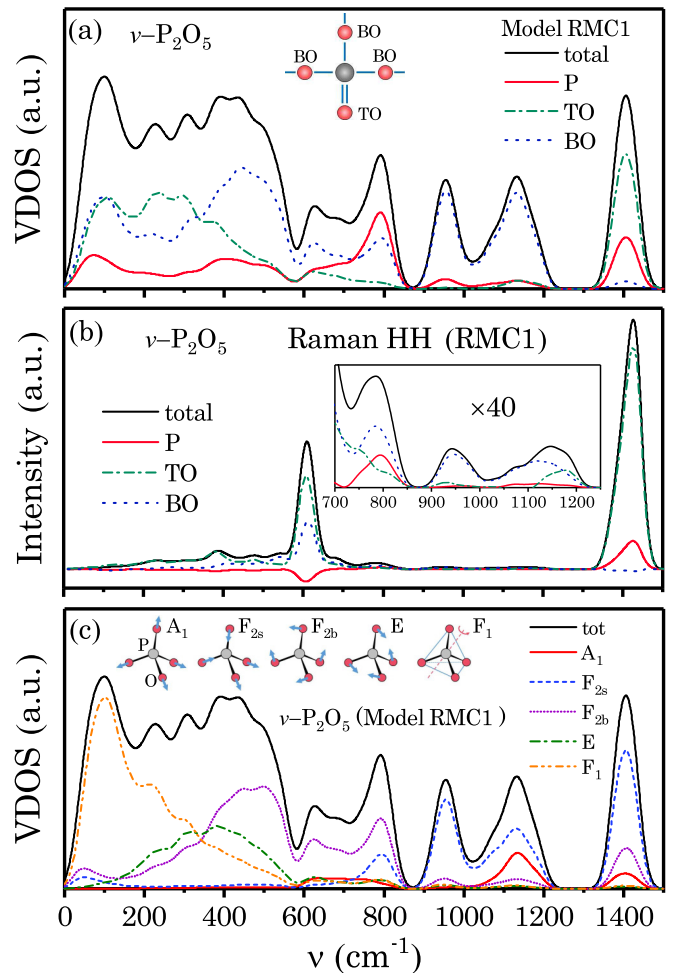

FIG. 8. (a) The partial VDOS for P atoms (solid red line), terminal oxygen (TO; dot-dashed green line) and bridging oxygen (BO; dotted blue line) atoms compared to the total VDOS (solid black line). The inset schematically shows the Q^3-PO$_4$ structural unit. (b) Deconvolution of the Raman HH spectrum with the same color code as in (a). The inset shows a zoom of intensity multiplied by a factor of 40 for the 700–1250-cm^{-1} frequency region. (c) The partial VDOS for the projections onto the T_d-group symmetries: A_1 symmetric stretching (solid red line), F_{2s} asymmetric stretching (dashed blue line), F_{2b} bending (dotted purple line), E bending (dot-dashed green line), and F_1 solid-unit rotations (double-dot-dashed orange line). The inset schematically shows the relative atomic displacements of the T_d group. The results are obtained for the RMC1 model.

compared with terminal oxygens [see Fig. 8(a)]; however, the polarizability of terminal oxygens is much stronger than that of bridging oxygens, which leads to their predominance in producing the Raman 640 cm^{-1} band [see Fig. 8(b)], and this assignment disproves the previous band attribution [14,16–18], which ascribed its origin mainly to the symmetric stretching modes of bridging oxygens. Also, we indicate comparable contributions of bridging oxygen and phosphorus motions and quite moderate contributions of terminal oxygens in the 700–870 cm^{-1} band; however, the phosphorus atoms contribute lightly to the Raman ∼800 cm^{-1} band [see the

inset in Fig. 8(b)]; that is, this Raman band is ascribed mainly to bridging oxygens. In the VDOS frequency range of 100–550 cm^{-1} it is interesting to note that terminal oxygens make a larger contribution than bridging oxygens in the range of 100–350 cm^{-1}, whereas the opposite is true in the range of 350–550 cm^{-1}. It is also interesting to mention that Raman spectra appearing at 100–550 cm^{-1} have a structure similar to the VDOS; however, the terminal oxygen contribution is decisive [see Fig. 8(b)] due to higher polarizability, and hence, the Raman modes in the range of 350–550 cm^{-1} are not specifically related to the bending modes of bridging oxygens [14,16].

Finally, we present a *full* tetrahedral (T_d) symmetry group analysis [20,21]. In Fig. 8(c), the spectrum in the range from ~600 to 870 cm^{-1} is dominated by bending (F_{2b}) motions related mostly to bridging oxygen and phosphorus (~800 cm^{-1} band) atoms [see Fig. 8(a)], while the high-frequency doublet zone (~870–1250 cm^{-1}) is associated mostly with the symmetric (A_1) and asymmetric (F_{2s}) stretching modes. One can note that the Raman bands ~870–1250 cm^{-1} behave silently, which complicates accurate measurements and analysis, whereas the IR spectrum shows strong resonances, especially at ~950 cm^{-1}. Since the modes above ~870 cm^{-1} are quite spatially localized (PR ~0.2), we are able to infer information about the intermediate range order (interbonding angle) [51], and hence, in the case v-P$_2$O$_5$, the IR spectroscopy seems to be preferred to Raman spectroscopy in this frequency range. The most prominent peak around 1400 cm^{-1} (experiment: 1380 cm^{-1}) is mainly due to asymmetric stretching vibrations of terminal oxygens, and its signatures are comparably strong in all vibrational spectra (see Fig. 5). The lower-frequency range in the VDOS below 600 cm^{-1} is shown to arise from a mixture of bending (E and F_{2b}) and rotation (F_1) modes. However, the scissors bending (E) and rotation (F_1) modes are well localized below 600 cm^{-1}, whereas the F_{2b} bending modes spread farther into the range of ~600–870 cm^{-1}. The boson peak area, i.e., <100 cm^{-1}, originates mostly from the rotation (F_1) modes, similar to v-SiO$_2$ [20,21]. It should be noted that our mode-projection analysis can be applied for other point symmetry groups, thus offering a powerful mode assignment tool, and hence unveils a more comprehensive methodology for studying vibrational properties in disordered systems.

IV. CONCLUSION

In conclusion, we presented a comprehensive analysis based on *ab initio* calculations and experimental measurements which provides an assignment of the Raman, IR, and VDOS spectra in v-P$_2$O$_5$ to vibrations of specific network structural units. Our analysis yields compelling evidence of the existence of only Q^3 tetrahedral units in pure v-P$_2$O$_5$. We have revealed in detail the internal structure of vibrations using a mode-projection analysis based on chemical species and the T_d symmetry group. Thus, this work serves as an exemplary study of disordered material with complex bonding configurations, and the combined modeling approach based on RMC and DFT simulations with mode-projection analysis is very promising for further studies of amorphous materials.

APPENDIX: RAMAN DECOMPOSITION

The Raman cross section is calculated assuming nonresonant conditions in the Placzek approximation, as described in a previous work [25] and given by (in esu)

$$\mathcal{I}^P(\nu) = \frac{2\pi h}{\nu} \frac{g(\nu)(\nu_L - \nu)^4}{V^{-1}c^4} \sum_k \mathcal{I}_k \delta(\nu - \nu_k), \quad \text{(A1)}$$

where the index k labeling the vibrational modes runs from 1 to $3N_{at}$, N_{at} is the total number of atoms in the models, ν_L is the frequency of the incoming photon, h is Planck's constant, c is the speed of light, V is the volume of the scattering sample, $g(\nu) = n_B(\nu) + 1$, and $n_B(\nu)$ is the boson factor. In this work, we give the Raman intensities using the following reduced expression:

$$\mathcal{I}(\nu) = \nu(\nu_L - \nu)^{-4} g^{-1}(\nu) \mathcal{I}^P(\nu). \quad \text{(A2)}$$

In experimental setups, it is customary to record the Raman spectra in the horizontal-horizontal (HH) configuration in which the polarization of the outgoing photons is respectively parallel to the ingoing photon polarization. Using the isotropy of disordered solids, we express the contribution of the kth mode $\mathcal{I}_k$ to the HH Raman spectra as

$$\mathcal{I}_k^{HH} = a_k^2 + \frac{4}{45} b_k^2. \quad \text{(A3)}$$

Below, we adapt the Umari and Pasquarello approach in Ref. [49] to take into account the interference effect and to additively decompose the Raman spectrum given by Eq. (A2) into partial contributions of specific groups of atoms $\{A_m\}$ ($m = 1, 2, 3$), $A_m \in \{P, TO, BO\}$, i.e., $\mathcal{I}(\nu) = \sum_m \mathcal{I}_{A_m}(\nu)$. The Raman susceptibility tensors $\mathbf{R}^k$ are given by

$$\mathbf{R}^k = \sum_m \mathbf{R}_{A_m}^k = \sum_m \left\{ \sqrt{V} \sum_{I \in A_m} \frac{\partial \boldsymbol{\chi}}{\partial \mathbf{R}_I} \frac{\mathbf{e}_I^k}{\sqrt{M_I}} \right\}, \quad \text{(A4)}$$

where χ is the electric polarizability tensor, the capital Latin index I runs over the atoms, and $\mathbf{R}_I$ and M_I are the position and the atomic mass of atom I, respectively. By using $\mathbf{R}_{A_m}^k$ we decompose a_k^2 and b_k^2 as follows:

$$a_k = \sum_m a_{k,A_m} = \sum_m \left\{ \frac{1}{3} \sum_{i=1}^{3} \mathcal{R}_{ii,A_m}^k \right\} = \frac{1}{3} \sum_{i=1}^{3} \mathcal{R}_{ii}^k, \quad (A5)$$

$$a_k^2 = \sum_m \tilde{a}_{k,A_m}^2 = \sum_m \sum_{m'} a_{k,A_m} a_{k,A_{m'}}, \quad (A6)$$

$$b_k^2 = \sum_{i<j} \left\{ \frac{1}{2} \left(\mathcal{R}_{ii}^k - \mathcal{R}_{jj}^k \right)^2 + 3 \left(\mathcal{R}_{ij}^k \right)^2 \right\}$$

$$= \sum_{i<j} \left(\gamma_{ij}^k \right)^2 + \sum_{i<j} \left(\delta_{ij}^k \right)^2 = \gamma_k^2 + \delta_k^2, \quad (A7)$$

where γ_{ij}^k and δ_{ij}^k are represented as

$$\gamma_{ij}^k = \sum_m \gamma_{ij,A_m}^k = \sum_m \frac{1}{\sqrt{2}} \left(\mathcal{R}_{ii,A_m}^k - \mathcal{R}_{jj,A_m}^k \right), \quad (A8)$$

$$\delta_{ij}^k = \sum_m \delta_{ij,A_m}^k = \sum_m \sqrt{3} \mathcal{R}_{ij,A_m}^k \quad (A9)$$

and γ_k^2 and δ_k^2 are decomposed as

$$\gamma_k^2 = \sum_m \tilde{\gamma}_{k,A_m}^2 = \sum_m \sum_{i<j} \sum_{m'} \gamma_{ij,A_m}^k \gamma_{ij,A_{m'}}^k, \quad (A10)$$

$$\delta_k^2 = \sum_m \tilde{\delta}_{k,A_m}^2 = \sum_m \sum_{i<j} \sum_{m'} \delta_{ij,A_m}^k \delta_{ij,A_{m'}}^k. \quad (A11)$$

By using Eqs. (A5)–(A11) we decompose $\mathcal{I}_k^{HH}$ as $\mathcal{I}_k^{HH} = \sum_m \mathcal{I}_{A_m,k}^{HH}$, which allows us to compute the mth terms $\mathcal{I}_{A_m}(\nu)$ representing the total intensity $\mathcal{I}(\nu)$ given by Eqs. (A2) and (3).

[1] N. G. Boetti, G. C. Scarpignato, J. Lousteau, D. Pugliese, L. Bastard, J.-E. Broquin, and D. Milanese, J. Opt. **17**, 065705 (2015).

[2] J. H. Campbell and T. I. Suratwala, J. Non-Cryst. Solids **263–264**, 318 (2000).

[3] N. Boetti, D. Pugliese, E. Ceci-Ginistrelli, J. Lousteau, D. Janner, and D. Milanese, Appl. Sci. **7**, 1295 (2017).

[4] P. D. Dragic, M. Cavillon, and J. Ballato, Appl. Phys. Rev. **5**, 041301 (2018).

[5] Y. Petit, S. Danto, T. Guérineau, A. A. Khalil, A. Le Camus, E. Fargin, G. Duchateau, J.-P. Bérubé, R. Vallée, Y. Messaddeq, T. Cardinal, and L. Canioni, Adv. Opt. Technol. **7**, 291 (2018).

[6] S. W. Martin, Eur. J. Solid State Inorg. Chem. **28**, 163 (1991).

[7] U. Hoppe, G. Walter, A. Barz, D. Stachel, and A. C. Hannon, J. Phys.: Condens. Matter **10**, 261 (1998).

[8] U. Hoppe, R. Kranold, A. Barz, D. Stachel, and J. Neuefeind, Solid State Commun. **115**, 559 (2000).

[9] R. K. Brow, J. Non-Cryst. Solids **263–264**, 1 (2000).

[10] I.-H. Jung and P. Hudon, J. Am. Ceram. Soc. **95**, 3665 (2012).

[11] V. V. Brazhkin, Y. Katayama, A. G. Lyapin, and H. Saitoh, Phys. Rev. B **89**, 104203 (2014).

[12] A. Ziletti, A. Carvalho, P. E. Trevisanutto, D. K. Campbell, D. F. Coker, and A. H. Castro Neto, Phys. Rev. B **91**, 085407 (2015).

[13] L. Giacomazzi, L. Martin-Samos, A. Alessi, N. Richard, A. Boukenter, Y. Ouerdane, S. Girard, M. Valant, and S. De Gironcoli, Sci. Rep. **9**, 7126 (2019).

[14] F. L. Galeener and J. C. Mikkelsen, Jr., Solid State Commun. **30**, 505 (1979).

[15] W.-B. Chang, Z.-Z. Jin, and X.-W. Zou, Phys. Lett. A **159**, 361 (1991).

[16] H. Mohmoh, M. Ouchetto, M. Couzi, J. P. Chaminade, E. Arbib, and B. Elouadi, Phosphorus Res. Bull. **13**, 187 (2002).

[17] G. Guimbretière, D. Bégué, M. Dussauze, and V. Rodriguez, Vib. Spectrosc. **63**, 426 (2012).

[18] F. L. Galeener and A. C. Wright, Solid State Commun. **57**, 677 (1986).

[19] J. J. Hudgens, R. K. Brow, D. R. Tallant, and S. W. Martin, J. Non-Cryst. Solids **223**, 21 (1998).

[20] S. N. Taraskin and S. R. Elliott, Phys. Rev. B **56**, 8605 (1997).

[21] N. S. Shcheblanov, M. E. Povarnitsyn, S. N. Taraskin, and S. R. Elliott, Phys. Rev. B **94**, 099903(E) (2016).

[22] J. Sarnthein, A. Pasquarello, and R. Car, Science **275**, 1925 (1997).

[23] M. Lazzeri and F. Mauri, Phys. Rev. Lett. **90**, 036401 (2003).

[24] G. Ferlat, T. Charpentier, A. P. Seitsonen, A. Takada, M. Lazzeri, L. Cormier, G. Calas, and F. Mauri, Phys. Rev. Lett. **101**, 065504 (2008).

[25] L. Giacomazzi, P. Umari, and A. Pasquarello, Phys. Rev. B **79**, 064202 (2009).

[26] R. Mazzarello, S. Caravati, S. Angioletti-Uberti, M. Bernasconi, and M. Parrinello, Phys. Rev. Lett. **104**, 085503 (2010).

[27] D. Stachel, I. Svoboda, and H. Fuess, Acta Crystallogr. Sect. C **51**, 1049 (1995).

[28] E. Lippmaa, M. Maegi, A. Samoson, G. Engelhardt, and A. R. Grimmer, J. Am. Chem. Soc. **102**, 4889 (1980).

[29] Y. Suzuki, K. Takase, I. Akiyama, K. Suzuya, N. Umesaki, and N. Ohtori, Mater. Trans. **42**, 2242 (2001).

[30] D. K. Belashchenko, Russ. Chem. Rev. **66**, 733 (1997).

[31] J.-J. Liang, R. T. Cygan, and T. M. Alam, J. Non-Cryst. Solids **263–264**, 167 (2000).

[32] T. M. Alam, J.-J. Liang, and R. T. Cygan, Phys. Chem. Chem. Phys. **2**, 4427 (2000).

[33] R. K. Sistla and M. Seshasayee, J. Non-Cryst. Solids **349**, 22 (2004).

[34] R. I. Ainsworth, D. D. Tommaso, J. K. Christie, and N. H. de Leeuw, J. Chem. Phys. **137**, 234502 (2012).

[35] S. Kohara, J. Akola, H. Morita, K. Suzuya, J. K. R. Weber, M. C. Wilding, and C. J. Benmore, Proc. Natl. Acad. Sci. USA **108**, 14780 (2011).

[36] S. Kohara and P. S. Salmon, Adv. Phys.: X **1**, 640 (2016).

[37] O. Gereben, P. Jóvári, L. Temleitner, and L. Pusztai, J. Optoelectron. Adv. Mater. **9**, 3021 (2007).

[38] S. Plimpton, J. Comput. Phys. **117**, 1 (1995).

[39] J. P. Perdew and A. Zunger, Phys. Rev. B **23**, 5048 (1981).

[40] N. Troullier and J. L. Martins, Phys. Rev. B **43**, 1993 (1991).

[41] G. B. Bachelet, D. R. Hamann, and M. Schlüter, Phys. Rev. B **26**, 4199 (1982).

[42] L. He, F. Liu, G. Hautier, M. J. T. Oliveira, M. A. L. Marques, F. D. Vila, J. J. Rehr, G.-M. Rignanese, and A. Zhou, Phys. Rev. B **89**, 064305 (2014).

[43] S. Baroni, S. De Gironcoli, A. Dal Corso, and P. Giannozzi, Rev. Mod. Phys. **73**, 515 (2001).

[44] P. Giannozzi, S. Baroni, N. Bonini, M. Calandra, R. Car, C. Cavazzoni, D. Ceresoli, G. L. Chiarotti, M. Cococcioni, I. Dabo *et al.*, J. Phys.: Condens. Matter **21**, 395502 (2009).

[45] K. Meyer, A. Barz, and D. Stachel, Phys. Chem. Glasses **43**, 108 (2002).

[46] Y. K. Voron'ko, A. A. Sobol', and V. E. Shukshin, Inorg. Mater. **41**, 1097 (2005).

[47] K. Meyer, J. Non-Cryst. Solids **209**, 227 (1997).

[48] R. Haworth, G. Mountjoy, M. Corno, P. Ugliengo, and R. J. Newport, Phys. Rev. B **81**, 060301(R) (2010).

[49] P. Umari and A. Pasquarello, J. Phys.: Condens. Matter **15**, S1547 (2003).

[50] D. Kilymis, S. Ispas, B. Hehlen, S. Peuget, and J.-M. Delaye, Phys. Rev. B **99**, 054209 (2019).

[51] N. S. Shcheblanov, M. E. Povarnitsyn, K. N. Mishchik, and A. Tanguy, Phys. Rev. B **97**, 054106 (2018).